A Physically Based Algorithm for Non-Blackbody Correction of Cloud-Top Temperature and Application to Convection Study

CHUNPENG WANG

Department of Atmospheric, Oceanic and Space Sciences, University of Michigan, Ann Arbor, Michigan

ZHENGZHAO JOHNNY LUO

Department of Earth and Atmospheric Sciences, and NOAA Cooperative Remote Sensing Science and Technology Center, City College of New York, New York, New York

XIUHONG CHEN

Department of Atmospheric, Oceanic and Space Sciences, University of Michigan, Ann Arbor, Michigan

XIPING ZENG AND WEI-KUO TAO

Mesoscale Atmospheric Processes Laboratory, NASA Goddard Space Flight Center, Greenbelt, Maryland

XIANGLEI HUANG

Department of Atmospheric, Oceanic and Space Sciences, University of Michigan, Ann Arbor, Michigan

(Manuscript received 1 November 2013, in final form 17 March 2014)

ABSTRACT

Cloud-top temperature (CTT) is an important parameter for convective clouds and is usually different from the 11-μm brightness temperature due to non-blackbody effects. This paper presents an algorithm for estimating convective CTT by using simultaneous passive [Moderate Resolution Imaging Spectroradiometer (MODIS)] and active [*CloudSat* + *Cloud–Aerosol Lidar and Infrared Pathfinder Satellite Observations* (*CALIPSO*)] measurements of clouds to correct for the non-blackbody effect. To do this, a weighting function of the MODIS 11-μm band is explicitly calculated by feeding cloud hydrometer profiles from *CloudSat* and *CALIPSO* retrievals and temperature and humidity profiles based on ECMWF analyses into a radiation transfer model. Among 16 837 tropical deep convective clouds observed by *CloudSat* in 2008, the averaged effective emission level (EEL) of the 11-μm channel is located at optical depth ~0.72, with a standard deviation of 0.3. The distance between the EEL and cloud-top height determined by *CloudSat* is shown to be related to a parameter called cloud-top fuzziness (CTF), defined as the vertical separation between −30 and 10 dBZ of *CloudSat* radar reflectivity. On the basis of these findings a relationship is then developed between the CTF and the difference between MODIS 11-μm brightness temperature and physical CTT, the latter being the non-blackbody correction of CTT. Correction of the non-blackbody effect of CTT is applied to analyze convective cloud-top buoyancy. With this correction, about 70% of the convective cores observed by *CloudSat* in the height range of 6–10 km have positive buoyancy near cloud top, meaning clouds are still growing vertically, although their final fate cannot be determined by snapshot observations.

1. Introduction

Cloud-top temperature and cloud-top height are two important parameters to retrieve in the remote sensing of clouds. Passive IR remote sensing techniques are

Corresponding author address: Chunpeng Wang, Dept. of Atmospheric, Oceanic and Space Sciences, University of Michigan, 2455 Hayward St., Ann Arbor, MI 48109-2143.
E-mail: cpwang@umich.edu

DOI: 10.1175/JAMC-D-13-0331.1

sensitive to a finite layer near cloud tops. The thickness of the layer varies from case to case. Thus, solely using IR measurement is not enough to accurately locate the physical cloud top and to estimate the corresponding cloud-top temperature. Yet, precise knowledge of cloud-top temperature (CTT[1]) and cloud-top height (CTH) is crucial for analyzing certain cloud processes. For example, estimation of convective buoyancy and entrainment rates as described by Luo et al. (2010) requires a high degree of accuracy of simultaneous measurements of CTT and CTH. Several attempts have been made in the past to address the problem. Minnis et al. (1990) assumed a linear relationship between visible cloud top and the infrared cloud emission level and derived an empirical relationship to estimate physical cloud-top temperature using emittance derived from the equivalent radiating temperature. In a follow-up study, Minnis et al. (2008) analyzed observations from the *Cloud–Aerosol Lidar and Infrared Pathfinder Satellite Observation* (*CALIPSO*) and thermal infrared satellite imagery of the Moderate Resolution Imaging Spectroradiometer (MODIS), and concluded with an expression for the cloud-top altitude of optically thick ice clouds as a function of the emission level. Along a similar line, Sherwood et al. (2004) examined the relationship between thermal cloud-top heights derived from geostationary satellite infrared imageries and direct measurements using airborne lidar observations and showed that the thermal cloud top is consistently ~1 km lower than the lidar cloud top. The aforementioned studies heavily rely on lidar and infrared brightness temperature. Lidar cannot penetrate deep into clouds. Although it can accurately determine the cloud top, lidar has difficulties in probing the in-cloud structure, especially for the convective core and thick anvils. Including simultaneous radar measurements will be helpful because radar can better profile thick clouds. Therefore, we pursue radar–lidar synergy in this study.

A common approach for inferring the cloud-top temperature of opaque clouds from IR passive remote sensing is to use the brightness temperature in the IR window region, typically over the 11-μm band (BT_{11}). The BT_{11} is a function of the temperature at cloud top as well as temperatures within a layer below due to the non-blackbody effect of clouds. However, the vertical structure of cloud microphysics [such as cloud water content (CWC)] near the cloud top varies from one cloud to another, affecting the depth of the layer over which IR measurements can penetrate. Some cloud tops are fuzzy with small cloud water content (moderate vertical gradient in optical depth) while others are compact with large cloud water content (large vertical gradient in optical depth). *CloudSat*, a spaceborne 94-GHz radar in operation since July 2006, is able to profile cloud structure with high vertical resolution and is also able to directly determine the cloud top. Its inability to detect small cloud particles near the top is complemented by the two-wavelength polarization-sensitive lidar aboard *CALIPSO* (Winker et al. 2009). Furthermore, *CloudSat*, *CALIPSO*, and MODIS aboard *Aqua* as part of the A-Train constellation (Stephens et al. 2002) make almost simultaneous observations. These facts motivate this study to explore how the vertical structure near cloud top is related to BT_{11} and how passive and active remote sensing measurements (viz., *CloudSat*, *CALIPSO*, and MODIS) can be used together to estimate CTT for optically thick clouds.

The motivation articulated in the previous paragraph is illustrated by two convective clouds in Fig. 1 with *CloudSat* radar reflectivity (dBZ) profiles in color scale and the natural logarithm of ice water content (IWC) derived from the combination of *CloudSat* and *CALIPSO* in grayscale. The vertical profiles of optical depth for the MODIS 11-μm channel are calculated using vertical profiles of CWC retrieved by *CloudSat* and *CALIPSO* (see section 2 for calculation details). From top to bottom, the black contour lines show the 11-μm optical depths (τ_{11}) of 0.5, 1, 5, and 20, respectively. The red plus signs mark the effective emission levels (EELs), which are defined as the altitudes corresponding to the peaks of the weighting functions of the MODIS 11-μm channel. Both radar reflectivity and cloud optical depth in Fig. 1 suggest that the convective cloud on the left has a more compact top than the one on the right. For the convective cloud on the right, the cloud-top fuzziness (as measured by the vertical gradient of radar reflectivity or optical depth) varies across the cloud. Consequently, the distance between the EEL (the red plus signs) and the radar cloud top is larger where the cloud-top layer is fuzzier and smaller where the cloud-top layer is more compact. Hereinafter, cloud tops are always defined as the altitude where the *CloudSat* radar reflectivity first reaches its detection limit, ~−30 dBZ. Such correlation between the vertical gradient of *CloudSat* radar reflectivity and the vertical gradient of 11-μm optical depth will be explored quantitatively in this study to better estimate physical cloud-top temperature. Current spaceborne cloud remote sensing provides the capability to capture the vertical profiles of radar reflectivity (e.g., *CloudSat*) and lidar backscatter (e.g., *CALIPSO*) but not the profiles of

[1] Hereinafter, CTT refers to the physical temperature at cloud top, not the brightness temperature, as is commonly the case in the literature.

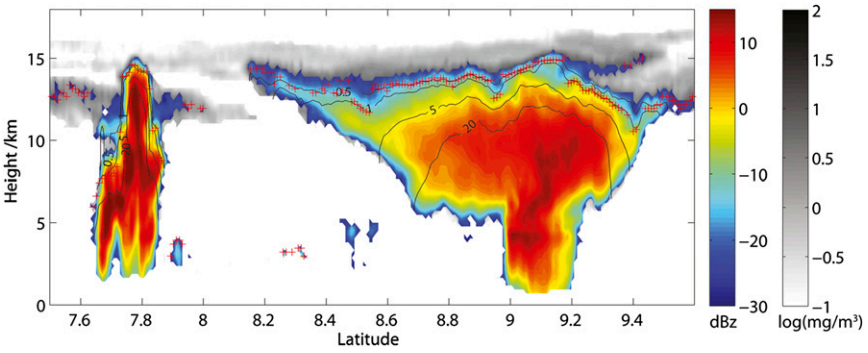

FIG. 1. *CloudSat* radar reflectivity (dBZ) observed at 0637 UTC 10 Oct 2008 is shown (colors) and the natural logarithm of cloud ice water (mg m^{-3}) content (grayscale). The black contour lines (from topmost to the bottommost) are for IR optical depths of 0.5, 1, 5, and 20, respectively. The red plus signs mark the levels with maximum weighting functions (the effective emission levels). This is the same event as Fig. 3 in Wang et al. (2011).

11-μm optical depth; yet it is the latter quantity that is most directly related to the IR determination of cloud-top temperatures.

To complement the analysis of observational data, three-dimensional (3D) cloud-resolving model simulations are used to provide a more complete understanding of the relationship. Specifically, the Goddard Cumulus Ensemble model (GCE; e.g., Zeng et al. 2009) is employed to simulate clouds and precipitation, driven by the large-scale forcing obtained from a field campaign. The GCE simulations are analyzed for studying detailed in-cloud structures that are elusive to satellite measurements (e.g., in-cloud temperature profile), aiming at a physically based understanding of the relationship among cloud-top temperature, BT_{11}, and *CloudSat* radar reflectivity.

The present paper is organized as follows. Section 2 introduces the datasets, GCE model, and radiative transfer calculations used in the study. Section 3 describes results obtained by examining collocated *CloudSat*, *CALIPSO*, and MODIS observations and analyzing radiative transfer model simulations. Section 4 analyzes the results from the GCE model simulations. Section 5 discusses the application to the convective buoyancy study. Section 6 presents a summary and conclusions.

2. Observations, models, and data processing

a. Observations

1) CLOUDSAT AND CALIPSO

The potential benefits of combining cloud-profiling radar and lidar together to probe clouds have been well recognized (Sassen et al. 2009; Luo et al. 2010, 2011; Young et al. 2012). Because the lidar on *CALIPSO* and the cloud-profiling radar (CPR) on *CloudSat* utilize different wavelengths, they are sensitive to cloud particles of different sizes. The lidar is operating in the visible wavelength and is able to detect thin cirrus cloud and aerosols but its laser pulse is strongly attenuated by optically thick cloud. The *CloudSat* radar, on the other hand, can typically sense and penetrate nonprecipitating cloud but can barely detect the thin cirrus with small particle sizes. Therefore, combining information from lidar and radar allows for a more complete description of the geometrical and microphysical parameters of clouds, given the wide varieties of size distribution of cloud particles within clouds (McGill et al. 2004; Minnis et al. 2012; Okamoto et al. 2003). For this reason, we use a joint *CloudSat–CALIPSO* product, whenever possible, to study cloud-top properties in this study. *CloudSat* and *CALIPSO* fly at an altitude of 705 km in a sun-synchronous polar orbit and make equatorial passes at approximately 0130 and 1330 local time (LT). The 94-GHz nadir-viewing CPR on board *CloudSat* profiles clouds with a vertical resolution of 480 m oversampled to 240 m and its ground footprint is approximately 1.7 km along track and 1.3 km cross track (Stephens et al. 2008). *CALIPSO*'s payload consists of an imaging infrared radiometer, a wide-field-of-view camera, and a two-wavelength lidar with the ability to resolve the orthogonally polarized components of the 532-nm backscattered signal. The lidar backscatter signal can profile clouds up to an optical depth of about 3 with a resolution of 60 m in vertical and 333 m in horizontal.

The following *CloudSat–CALIPSO* data products are used, all obtained from the *CloudSat* Data Processing Center (http://www.cloudsat.cira.colostate.edu/): 1) 2B-GEOPROF, the *CloudSat* geometric profile product, provides the CPR radar reflectivity profiles and is used in this study to identify cloud tops and to quantify the fuzziness of cloud-top layer and 2) 2B-CWC-RVOD and

2C-ICE provide cloud microphysics parameters such as CWC, which is used as the input for radiative transfer model calculations. The 2C-ICE product is based on the joint retrieval from collocated *CloudSat* and *CALIPSO* measurements and provides ice water content (Deng et al. 2010). The 2B-CWC-RVOD product has both liquid water content (LWC) and IWC, but the information content is largely derived from the *CloudSat* CPR and constrained by MODIS visible optical depth (Wood 2008). Deng et al. (2013) show that 2C-ICE outperforms 2B-CWC-RVOD in cloud ice microphysics retrieval, underscoring the importance of radar–lidar synergy in ice cloud property retrievals. To take advantage of the radar–lidar synergy, we used the 2C-ICE product for IWC profiles. The 2B-CWC-ROVOD data are used only for its LWC profiles.

We define a parameter that will later be used to measure the near-cloud-top conditions, which we call cloud-top fuzziness (CTF):

$$\mathrm{CTF} = \mathrm{CTH} - \mathrm{ETH}_{10\mathrm{dB}Z}, \tag{1}$$

where CTH (cloud-top height) is defined based on the *CloudSat* CPR corresponding to the height of −30 dBZ, and $\mathrm{ETH}_{10\mathrm{dB}Z}$ (echo-top height) is the highest altitude reached by 10 dBZ. The 10-dBZ echo is an indicator of the presence of large precipitation-size particles and thus $\mathrm{ETH}_{10\mathrm{dB}Z}$ is a good proxy for convective strength (Luo et al. 2008, 2011). CTF so defined thus measures the extent to which precipitation-sized particles are transported to near the cloud top. The smaller the CTF, the more compacted the cloud top is, and vice versa. It will be shown later that CTF is closely related to the correction for the IR non-blackbody effect.

2) MODIS

MODIS aboard *Aqua* flies in close formation with *CloudSat*, being separated from each other by a variable time interval that is always less than 120 s. It measures narrowband radiances in 36 spectral bands from 0.415 to 14.24 μm with wavelength-dependent nadir spatial resolutions from 250 m to 1 km in a 2300-km-wide swath (King et al. 1992; Platnick et al. 2003). The 11-μm brightness temperature, BT_{11}, from the *Aqua* MODIS measurement is collocated to *CloudSat* observations after the correction of the parallax shift following the method depicted in Wang et al. (2011).

3) ANALYSIS OF OBSERVATIONAL DATA

The ambient temperature and relative humidity are obtained from the *CloudSat* ECMWF-AUX dataset and are inputted into the radiative transfer simulation. ECMWF-AUX is based on European Centre for Medium-Range Weather Forecasts (ECMWF) operational analyses, spatially and temporally interpolated to the *CloudSat* track. Note that the optical depth in *CloudSat* level-2 product, the *CloudSat* 2B-TAU, is for 0.55 μm, which is different from the 11-μm optical depth used throughout this study. We calculate the 11-μm optical depth using the Principal Component-Based Radiative Transfer Model (PCRTM), a radiative transfer model that is described in section 2c.

All *CloudSat* data and 2C-ICE retrievals collected within the tropics (30°S–30°N) during 2008 are analyzed here. We choose convective clouds by the criteria that 1) CTF is less than 4 km and 2) CTH is greater than 6 km such that boundary layer convective clouds are excluded. As a result, 277 968 profiles (0.43% of total *CloudSat* observations in the tropics) meet our criteria. To best capture the behavior of the core of convection, for each strong convective cloud that has consecutive *CloudSat* radar echo profiles that meet our criteria, we only use the one with the highest CTH considering that it is likely to be closer to the actual convective core. This reduces our selected profiles to a total of 16 837 for the following analysis. Figure 1 shows two examples of the selected convective clouds. More details related to the selection of the convective clouds can be found in Wang et al. (2011).

b. Goddard Cumulus Ensemble (GCE) model

The GCE model is a cloud-resolving model that has been developed at the National Aeronautics and Space Administration (NASA) Goddard Space Flight Center over the past few decades (e.g., Tao and Simpson 1993; Tao et al. 2003) and is extensively used to study cloud processes and their interactions with the environment. The model is nonhydrostatic and anelastic. Its subgrid-scale turbulent processes are parameterized with a scheme based on the work of Klemp and Wilhelmson (1978) and Soong and Ogura (1980). The model includes solar and infrared radiative transfer processes, and explicit cloud–radiation interaction processes. The model has five prognostic hydrometeor variables: the mixing ratios of cloud water, rainwater, cloud ice, snow, and graupel [see Tao and Simpson (1993), Tao et al. (2003), and Lang et al. (2003) for details].

In this study, GCE simulations are used as a surrogate for real convective cloud development processes. The model is driven by the large-scale tendencies observed in the Tropical Warm Pool International Cloud Experiment (TWP-ICE; May et al. 2008), and uses 256 × 256 horizontal grid points at 1-km resolution. Its modeling results have been evaluated with C- and W-band radar data, as well as satellite data (Zeng et al. 2013).

The TWP-ICE simulation analyzed here lasts for 6 days (6~12 February 2006) and 2429 simulated convective cores are identified in total. All the information on those cores is fed into QuickBeam (see section 2c) to simulate the 94-GHz radar reflectivity that mimics *CloudSat* CPR from a nadir view. In addition, PCRTM, a fast and accurate thermal radiative transfer model, is used to simulate MODIS BT_{11}, as well as the vertical profile of the optical thickness for the same MODIS viewing zenith angle. The emission level is then derived by calculating the corresponding weighting function and by locating its peak.

The cloud selection method for observational data analysis is applied similarly to the model simulations. Specifically, convective clouds are selected for analysis if their CTH ranges from 6 to 18 km and is within 4 km of the simulated ETH_{10dBZ}. Similar to the data selection process for satellite measurements, the simulated profile at one model grid is used to represent the core of a convective cloud. A convective core in the model is defined based on the following criteria: 1) grid points are classified as a convective region by GCE, 2) maximum upward velocity exceeds 2 m s^{-1}, 3) outgoing longwave radiation is less than 210 W m^{-2}, 4) integrated water path is greater than 0.5 cm, and 5) simulated MODIS BT_{11} by PCRTM is less than 270 K. Each convective core is treated as one entity, and for a cluster of neighboring cores, the one with the largest cloud water content is used to represent them for further analysis, similar to the analysis as described in section 2a.

c. *QuickBeam, PCRTM, and model-to-satellite simulation strategy*

GCE outputs such as mixing ratios of cloud hydrometeors are fed into the QuickBeam simulator (Haynes et al. 2007) to derive synthetic *CloudSat* radar reflectivities. This ensures a consistent method of defining the CTT and ETH between model simulations and observations. In this study, the mixing ratios of the five kinds of hydrometeor species in GCE are specified for the QuickBeam. To be consistent with the intrinsic size distribution of the GCE (Tao and Simpson 1993), snow, graupel, and rainwater are assumed to have an exponential size distribution; cloud water and cloud ice are assumed to be monodisperse in the QuickBeam simulator.[2] The scattering and absorption by atmospheric gases and thus gaseous attenuation of the radar beam are taken into account. Therefore, with the output of the radar echo, CTT and ETH for clouds in GCE simulations can be similarly defined, bridging the gap between *CloudSat* observations and GCE simulations.

PCRTM (Liu et al. 2006) is now becoming a widely used atmospheric radiative transfer model in the IR remote sensing community thanks to its computational efficiency and accuracy. Unlike channel-based radiative transfer models, PCRTM computes the principal component scores of the channel radiance, which greatly improves the computational efficiency. The benchmark comparison with a line-by-line radiative transfer model also shows that PCRTM performs satisfactorily in terms of accuracy. Further technical details about the PCRTM can be found in Liu et al. (2006, 2009). Multiple scattering is incorporated into PCRTM by including a precalculated lookup table of the reflectance and transmission of clouds using discrete-ordinate-method radiative transfer (Stamnes et al. 1988). Single-scattering properties are obtained from Yang et al. (2001), Wei et al. (2004), and Niu et al. (2007) by averaging the single-scattering properties The complex refractive indexes of ice are taken from Warren (1984), with his 1995 update, and that of water from Segelstein (1981).

The PCRTM is used here for two purposes: 1) to calculate BT_{11} with inputs from vertical profiles of cloud water content, temperature, and humidity, and 2) to calculate the IR transmissivity of each discretized vertical layer. For simulating BT_{11} using *CloudSat* and *CALIPSO* observations, inputs into the PCRTM are taken from the IWC profile from the *CloudSat* 2C-ICE product, and temperature and humidity profiles from the ECMWF operational analysis. For simulating BT_{11} using GCE simulations, the GCE output of the same variables is directly fed into the PCRTM. PCRTM calculation is done at a spectral resolution of 1 cm^{-1} (full width at half maximum) and the result is then convolved with the spectral response function of the MODIS 11-μm band (available online at http://mcst.gsfc.nasa.gov/calibration/parameters). In this work, a sensor-viewing zenith angle is set to match those of collocated MODIS observations. To ensure enough vertical resolution to accurately identify the peak altitude of the weighting function, the transmissivity is calculated for every 50-m interval in the troposphere. Temperature and humidity profiles above the cloud top are taken from the ECMWF-AUX data products. The relative humidity was set to 100% whenever hydrometeors were present. For *CloudSat–CALIPSO*–MODIS-related analyses, treatment of the in-cloud temperature profiles in the PCRTM modeling needs some further assumptions and will be described in detail in the next section. For the GCE simulation, no assumption is needed for in-cloud

[2] These size distributions are applied to maximize the consistency with the GCE output. We note here that the size distribution of hydrometeors in reality could be much more complicated than the one assumed in the QuickBeam simulator.

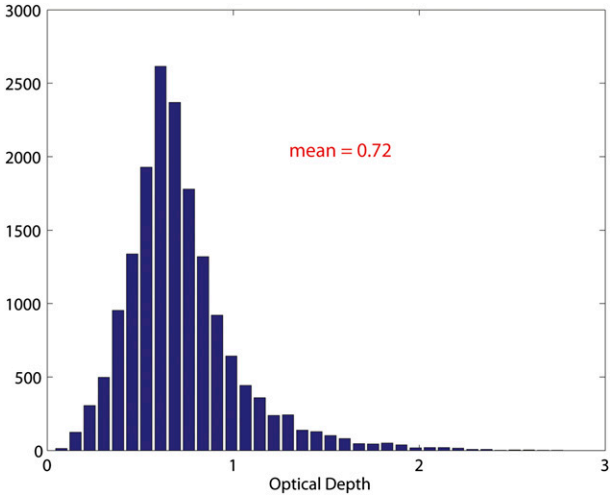

FIG. 2. Histogram of the effective emission level (the peak of the weighting function) expressed in the 11-μm optical depth. The histogram indicates the mean effective emission level is at an IR optical depth of 0.72.

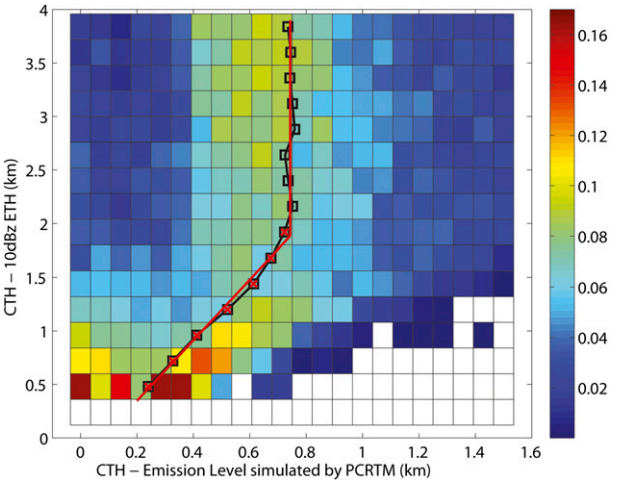

FIG. 3. The 2D histogram of the distance between CTH and the EEL computed by PCRTM (abscissa) vs the distance between CTH and $\mathrm{ETH}_{10\mathrm{dBZ}}$ (ordinate). The figure is normalized for each CTH − $\mathrm{ETH}_{10\mathrm{dBZ}}$ interval. The black squares show the expected distance between CTH and EEL from such probability distributions. The red line is the regressed results.

profiles since everything is available from the GCE direct output. The BT_{11} at the top of atmosphere and the corresponding transmissivity at 50-m vertical resolution are obtained from PCRTM calculations. The latter is then numerically differenced to derive the weighting function. As mentioned in section 1, the EEL is then defined as the altitude where the weighting function attains its maximum.

3. Non-blackbody correction for the tropical deep convection

a. *Effective emission level and relation to cloud-top fuzziness*

We first numerically investigate the following question: Where is the peak of the weighting function for the IR window channel near 11 μm? While it is often assumed that the peak of the IR weighting function is located at the altitude where optical depth $\tau = 1$, this exact statement is either based on the assumption that the Planck function varies linearly with respect to optical depth with no scattering effect (Sherwood et al. 2004) or is based on other approximations about the absorption lines (Stephens 1994; Goody and Yung 1995). In this study, we use a full-fledged radiative transfer model, the PCRTM, to explicitly evaluate the peak of the weighting function in the presence of scattering inside clouds. Figure 2 shows the histogram of τ_{11} where the weighting function attains its maximum. Based on Fig. 2, the expected value of τ_{11} is 0.72 with a standard deviation of 0.3. Among all cases examined here, 99.4% have their weighting functions peaking at $\tau_{11} < 2$. The histogram is largely symmetric, except a for small tail beyond $\tau_{11} > 2$, which is found to be caused by interpolation of the cloud optical depth in the presence of an extremely large vertical gradient of cloud water content at the cloud top.

As shown in Fig. 1, the distance from cloud top identified by *CloudSat* to the EEL changes with the fuzziness of the cloud top. Figure 3 further demonstrates this with a 2D histogram showing the relationship between CTF and the distance from CTH to the EEL derived from the PCRTM calculation (denoted as x hereinafter). The quantity x is critical to the non-blackbody correction of the CTT. Figure 3 shows that it is related to *CloudSat* radar reflectivity profiles and thus can be parameterized using such measurements. The composite result $x = x(\mathrm{CTF})$ is shown as a black line with squares. The composite in Fig. 3 shows that, when CTF is smaller than ~2 km (i.e., relatively compact cloud top), x is nearly linearly proportional to CTF and, when CTF is more than ~2 km, the x composite becomes constant at ~0.74 km. This can be expressed mathematically as

$$x = \min\left(\frac{\mathrm{CTF} + b}{a},\ 0.74\right), \tag{2}$$

where the values of a and b are determined by the linear regression of the data. To assess the impact of the *CloudSat* 2C-ICE retrieval uncertainty on the values

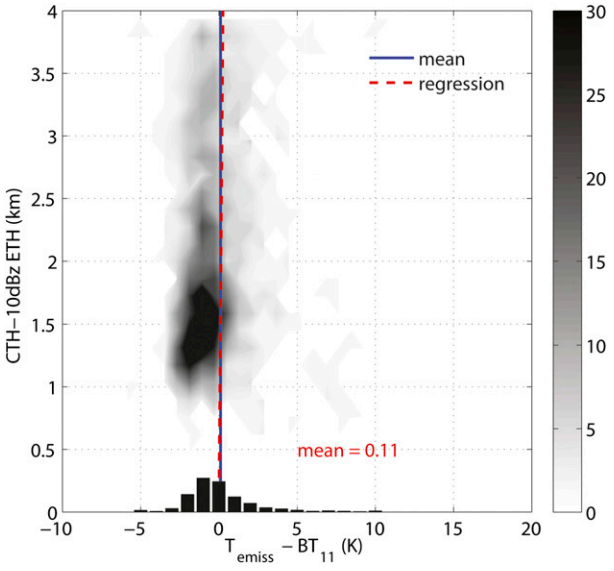

FIG. 4. Number density plot of GCE-simulated cases. Outliers beyond a 3-σ range are not included. Histogram is shown by the black bars. The red dotted line is the regression result, and the blue line is $T_{\mathrm{EEL}} - \mathrm{BT}_{11} = 0.11$ K.

of a and b, we randomly perturb IWC and LWC profiles with random numbers that follow normal distributions in accordance with the corresponding 2C-ICE retrieval uncertainties. Such perturbed profiles are then fed to QuickBeam and PCRTM to generate figure similar to Fig. 3, and then values of a and b are derived for this set of perturbations. We repeat such random perturbation calculations for 20 times and use them to estimate the uncertainty due to the retrieval uncertainty of IWC and LWC. In this way, $a = 2.83$ with a 1-σ uncertainty of 0.069 and $b = 0.22$ with a 1-σ uncertainty of 0.044.

b. *Temperature at the effective emission level versus* BT_{11}

To make the relation derived in Eq. (1) useful for estimating CTT, knowledge of the in-cloud temperature at the EEL, T_{EEL}, is needed. The value of T_{EEL} is slightly different from the actual BT_{11}, which is a weighted average of the in-cloud temperatures along a layer near cloud top. However, current remote sensing techniques cannot provide direct measurement of the vertical profile of in-cloud temperature; in situ measurements inside cumulonimbus are rare. So, we used GCE model simulations to investigate the differences between T_{EEL} and BT_{11}.

Results based on GCE simulations are presented in Fig. 4 as a number density plot with the ordinate representing the simulated CTF (=CTH – $\mathrm{ETH}_{10\mathrm{dB}Z}$) and the abscissa representing the difference between T_{EEL} and BT_{11}. Figure 4 shows that the $T_{\mathrm{EEL}} - \mathrm{BT}_{11}$ difference has an appreciable spread largely independent from CTF. The mean of the $T_{\mathrm{EEL}} - \mathrm{BT}_{11}$ difference is 0.11 K with a standard deviation of 2.3 K. Such spread could be due to a variety of factors such as the inclusion of multiple scattering in our radiative transfer calculation, the subtle variations of hydrometeor profiles near the cloud top as simulated by the GCE model, and so on. Based on a Student's t test, the 0.11-K mean difference is statistically different from zero at a significance level of 0.04. This small positive difference can be understood in the following way: ideally assuming temperature decreases linearly with altitude, the weighting function, largely bearing the shape of a Chapman function (Goody and Yung 1995, chapter 6), is slightly skewed to its upper tail. Therefore, as long as the effective emission level resides well below the tropopause, which is true for most cases except overshooting convection, BT_{11} could be considered to be slightly smaller than the temperature at the emission level. Nevertheless, it should be noted that 0.11 K is such a small difference when compared with the uncertainty of satellite measurement for cloud tops (Menzel et al. 2008) that BT_{11} can be treated as a good approximation of the T_{EEL} for convective clouds.

Based on these calculations, we arrive at the following expression to estimate cloud-top temperature based on MODIS BT_{11} and *CloudSat* measurements:

$$\mathrm{CTT} = \mathrm{BT}_{11} - \Gamma_m \min\left(\frac{\mathrm{CTF} + 0.22}{2.83}, 0.74\right) + 0.11\,\mathrm{K}, \tag{3}$$

where CTF is the cloud-top fuzziness in kilometer and Γ_m is the moist-adiabatic lapse rate around the top of the cloud in kelvins per kilometer. In physical terms, Eq. (3) states that the IR non-blackbody correction, namely the difference between CTT and BT_{11}, is proportional to the CTF parameter defined in section 2a: the fuzzier the cloud top (larger CTF), the greater the correction, and vice versa. It is also proportional to the in-cloud lapse rate Γ_m.

As far as uncertainties in Eq. (3) are concerned, the measurement uncertainty of BT_{11} is ~0.34 K (Xiong et al. 2009). For the second term on the right side of Eq. (3), its uncertainty is ~4 K given $\Gamma_m \sim 8\,\mathrm{K\,km^{-1}}$ at convective cloud top and the standard deviation of the emission level estimation ~0.5 km. The standard deviation of the $T_{\mathrm{EEL}} - \mathrm{BT}_{11}$ difference [i.e., the third term on the right side of Eq. (3)] is 2.3 K. Since the histograms in Figs. 3 and 4 can be viewed as empirical probability distribution functions (pdf), the uncertainty can be assessed in the following Monte Carlo way: for any given y

in Fig. 3, obtaining an estimate of x in Fig. 3 according to the empirical pdf determined by the histogram in Fig. 3. Similar steps apply for the $T_{EEL} - BT_{11}$ difference with the given standard deviation. Such an estimate will be used in Eq. (3) in lieu of the regression formula to get an estimate of the CTT. By repeating such an estimate many times, an uncertainty for the CTT estimated by Eq. (3) can be derived. The results using such a Monte Carlo approach will be presented later (Fig. 7).

4. Simulated versus observed BT_{11}

To gain more confidence in our non-blackbody correction for convective clouds, we compare BT_{11} from the PCRTM simulation with the observed BT_{11} from *Aqua* MODIS. The value of BT_{11} is simulated based on our estimation of CTT. The approach adopted here is backward in comparison with section 3; namely, we assume that CTT is known and then start from there to calculate BT_{11}. The rationale is to see if we can solve the problem both ways.

We compare two approaches in terms of estimating the in-cloud temperature profiles. One approach assumes no a priori knowledge of CTT and uses the ambient air temperature at the cloud-top level (taken from the ECMWF-AUX product) to represent the CTT and further assume the moist-adiabatic change of temperature inside the cloud. The color contours in Fig. 5a show the 2D histogram of the simulated and the observed BT_{11} following this assumption. The second approach assumes $BT_{11}+0.11$ K as the temperature at the EEL and calculates CTT according to Eq. (3). Note that the second approach does not require neutral cloud-top buoyancy (i.e., CTT equal to the ambient temperature). Black contour lines in Fig. 5a show the results from the second approach. The regressed slope of simulated BT_{11} versus MODIS BT_{11} is 0.995 for the first approach with R^2 of 0.96 and 1.004 for the second approach with R^2 of 0.99. To better illustrate the improvement, Figs. 5b and 5c show the 2D histograms of the differences between the simulated and measured BT_{11} with respect to MODIS BT_{11}, without and with our non-blackbody correction method, respectively. In contrast to Fig. 5b, Fig. 5c, with the correction, demonstrates that the second approach yields a tighter distribution and that the cases are better aligned at the zero-difference line, especially for the lower cloud. Therefore, we conclude that BT_{11} is better simulated when CTT is computed using our non-blackbody correction method, as opposed to assuming CTT equals the ambient air temperature. The small difference between CTT and the ambient air temperature is proportional to the convective buoyancy, as will be discussed in section 5.

Figure 5c shows that tropical convective clouds above the planetary boundary layer tend to cluster around two temperature ranges, namely, 250–265 and 200–220 K. They correspond to two equally obvious modes of convective clouds (Johnson et al. 1999): cumulus congestus and deep convection, as noted in Luo et al. (2010). Overall, Fig. 5 suggests that the observed BT_{11} can be largely reproduced given our knowledge of CWC and temperature profiles. This is encouraging and lends support to the validity of our method. There are also some noticeable biases. For example, there is a ~2-K warm bias for the black contours when BT_{11} is lower than 240 K (i.e., the deep convection mode). For $BT_{11} >$ 240 K (i.e., the cumulus congestus mode), the simulated BT_{11} is distributed closely along the red line with a warm bias of less than 0.5 K. The bias is larger for approach 1 (where CTT is assumed to equal that of the environment) than approach 2, especially for the cumulus congestus mode. A number of reasons could account for these biases. For example, the ECMWF analyses, which represent the large-scale environment, may not accurately capture the temperature profile near convective clouds, especially when convection triggers local diabatic and adiabatic processes that could influence the vertical temperature profile at the spatial scale comparable to the MODIS footprint.

5. Comparison with previous studies and application to studying convective buoyancy

An important reason why accurate knowledge of CTT is critical can be traced to a series of recent publications (Luo et al. 2008, 2010; Wang et al. 2011) that utilize the synergy between *CloudSat* and MODIS measurements to estimate convective buoyancy. Convective buoyancy (B) is proportional to the difference between CTT and the ambient air temperature of the same height level. Luo et al. (2010) concluded through a sensitivity and uncertainty test that CTT is the major source of error in convective buoyancy estimation. Even a merely 1–2-K error in CTT is large enough to affect the determination of the "fate" of some convective clouds, namely, whether they are bound to make further ascent or have already lost buoyancy.

In previous studies, Luo et al. (2010) and Wang et al. (2011) used a simple, empirical method to correct for nonblack cloud-top emissivity as follows: since *CALIPSO*'s lidar signal cannot penetrate beyond an optical depth at a visible wavelength τ_{vis} of ~3, this attenuation depth provides a means of estimating the correspondence between τ_{vis} and physical depth. It is further assumed that the effective IR emission level is located at $\tau_{IR} = 1$ and the relationship between τ_{vis} and τ_{IR} follows that

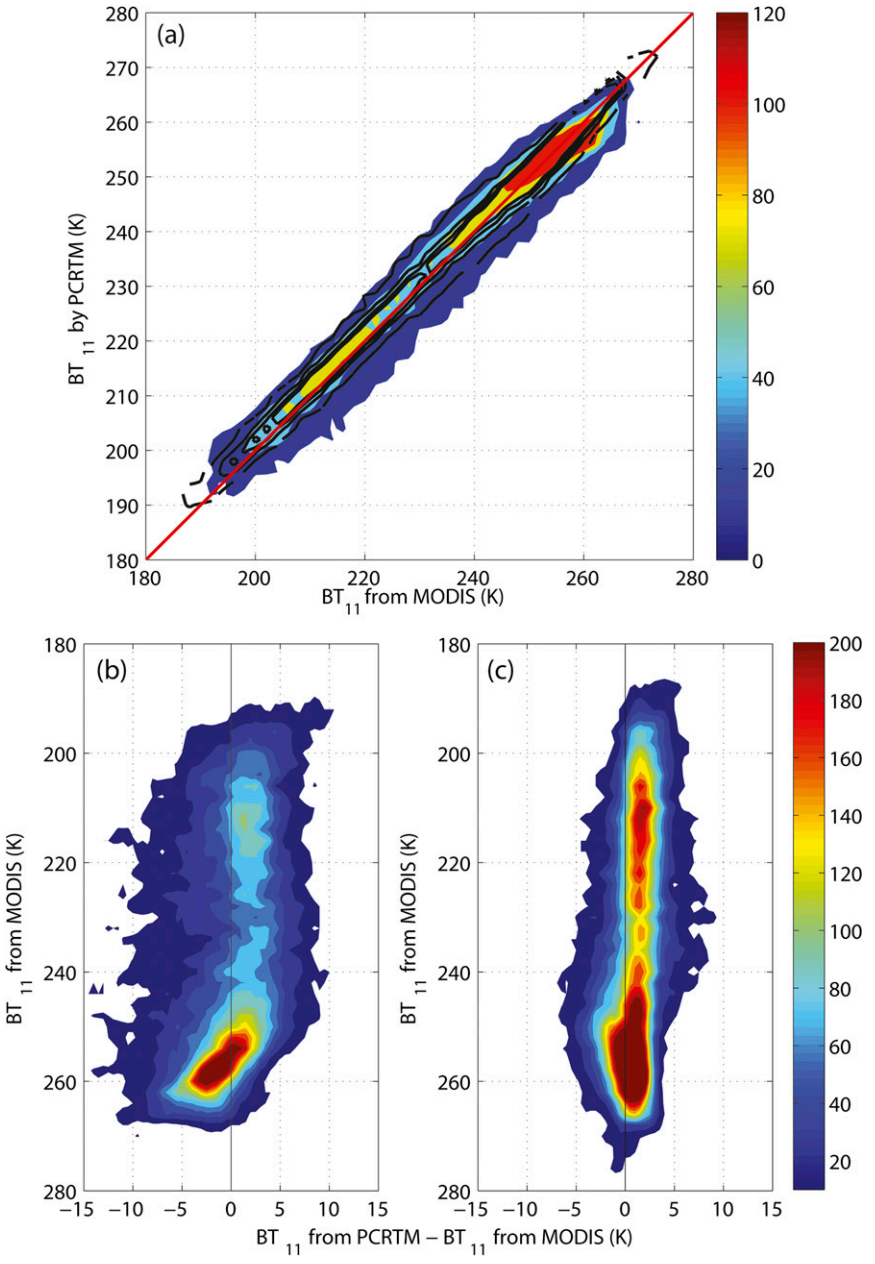

FIG. 5. (a) The 2D histogram of the numbers of occurrences of the 11-μm brightness temperature (BT_{11}) measured by MODIS (abscissa) and simulated using PCRTM with *CloudSat* cloud water profiles and temperature and humidity profiles as described in the text (ordinate). The red line with a slope of 1:1 is plotted as a reference. Color-filled contours are results assuming CTT equal to the ambient air temperature. The black contours are the result from updated estimation of CTT described in section 4. The difference between simulated BT_{11} and MODIS measurements with respect to MODIS BT_{11} (b) with and (c) without non-blackbody correction. The same color contours are used in (b) and (c).

provided by the International Satellite Cloud Climatology Project (ISCCP; Rossow et al. 1996): τ_{vis}/τ_{IR} = 2.56 for water clouds and 2.13 for ice cloud. Clearly, this correction method is rather crude. For example, the lidar penetration depth may deviate from τ_{vis} of 3 and τ_{vis} may not vary linearly with depth. Also, the effective IR emission level may not always occur at τ_{IR} = 1, as demonstrated in Fig. 2. Moreover, the visible-to-IR optical depth conversion is not a constant and may vary from one case to another. Nevertheless, it represented our first

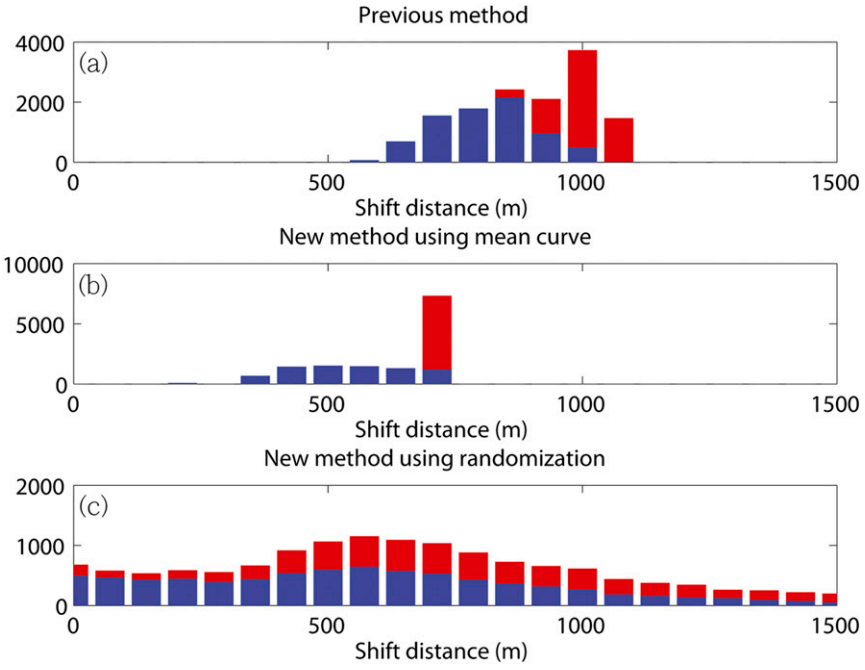

FIG. 6. Histogram of the distance between cloud top and EEL for all cases examined here. Blue bars show the histogram of cases with CTH − ETH_{10dBZ} < 2 km. The red bars are for cases with CTH − ETH_{10dBZ} within 2–4-km range. (a) Based on the previous method used in Luo et al. (2008). (b) Using Eq. (2) to compute such distances. (c) The empirical pdf based on Fig. 3 is used to estimate the distances (more details on this estimation can be found at the end of section 4).

attempt to address the problem. Here, we compare results derived from the previous method with those from this study, which is more physically based.

Figure 6 shows the histograms of the distance from cloud top to the EEL [i.e., x in Eq. (2)], as derived using three different methods. Figure 6a is based on the earlier method used in Luo et al. (2010) and Wang et al. (2011). Since Fig. 3 shows that the relationship changes from CTF < 2 km to CTF > 2 km because of the saturation of emission at that level, we divide the selected convective cases into two different groups: one has CTF less than 2 km and the other has CTF at 2–4 km. They are shown as blue and red bars in Fig. 6, respectively. In Fig. 6a, the blue histogram shows a peak around 0.8 km with a spread between 0.5 and 1 km. The red histogram reaches its maximum at around 1 km.

Figure 6b is based on Eq. (2): the spread of the blue histogram is similar to that of the bar histogram in Fig. 6a, but the peak of the histogram is now at 0.5 km. The expected emission level, as shown in Fig. 2, is where τ is ~0.72, instead of exactly 1 as assumed in the previous method. Therefore, the new non-blackbody correction should be smaller than that by Luo et al. (2010) and Wang et al. (2011), which leads to warmer CTTs than previous estimates.

Figure 6c is based on the estimates using the empirical PDF derived from Fig. 3 instead of Eq. (2), as explained in the last paragraph of section 3. Figure 6c shows wider spread for both groups than Fig. 6b, but their peaks are at similar locations and the expectation of the red histogram corresponds to the red bar in the middle panel. This can be explained by the fact that Fig. 6b is based on the regression values derived from Fig. 3 while Fig. 6c takes the entire spread in Fig. 3 into account. Hereinafter, the correction estimated from such an empirical PDF is denoted as PDF-based correction and the correction using Eq. (2) is referred to as regression-based correction.

As an application, the convective buoyancy as analyzed in Luo et al. (2010) and Wang et al. (2011) is reexamined. The convective cloud-top buoyancy is represented by the difference between CTT and the ambient air temperature (T_{env}) of the same level: $\Delta T \equiv \mathrm{CTT} - T_{env}$. Figure 7 presents the fraction of convection with positive buoyancy as a function of CTH from 6 to 18 km for both the new and old methods.[3]

[3] The corresponding figure in Wang et al. (2011) included a programming error that led to the incorrect estimation of the ratio of positive buoyancy. That error has been fixed here.

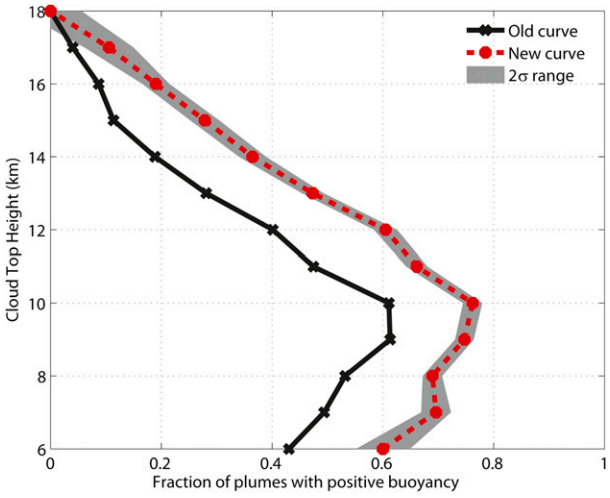

FIG. 7. Fraction of convection clouds with positive buoyancy as a function of CTT. The bin size of CTT is 1 km. The black line corresponds to the black line in Fig. 6 of Wang et al. (2011) with a small coding bug corrected. The red line is based on Eq. (3) and shows the fraction for all cases. The shaded area indicates the 2-σ range calculated on the basis of Figs. 3 and 4.

Taking ΔT as a proxy to show how vigorous the convection is, Fig. 7 suggests that tropical deep convection is statistically strongest when reaching 9–10 km and gradually loses momentum during further development due to the depletion of latent heat, entrainment of cold dry air, and overshooting the level of neutral buoyancy. These results can be explained by the observations of trimodal characteristics of tropical convection (Johnson et al. 1999). The smaller portion of the positive buoyancy at a CTH of 6 km is related to the existence of the weak stable layer, melting level at ~5 km. Many cumulus congestus do not glaciate fast enough and fail to gain enough thermal energy from latent heat release to sustain further upward motion. For the fast-glaciating clouds, they are likely to gain the maximum apparent heat at 8 km (Takayabu et al. 2010), get heated up during ascent, and achieve the strongest buoyancy at 9–10 km (~300 hPa). Because of this strong positive buoyancy, updraft motion is likely to continue and a local minimum of detrainment is thus expected, which is supported by Fig. 6b in Zuidema (1998).

The new IR non-blackbody correction method leads to more cases with positive cloud-top buoyancy for the very reason that the new correction is smaller than the old one, thus resulting in warmer CTT estimates (Fig. 6). Figure 7 shows that around 70% of the selected convective cores with tops lower than 10 km have positive buoyancy near cloud top, meaning that they will continue to accelerate. This result suggests that statistics collected from previous studies concerning convective clouds using polar-orbiting satellite data (i.e., snapshot observations) should be treated with caution. In particular, statistics on apparent cumulus congestus that have a lot of space to grow vertically (e.g., Casey et al. 2012) should be reassessed in light of our study. Our results thus underscore the importance of interpreting satellite snapshot observations within the proper dynamic context; that is, convective life stages need to be considered. In parallel to Wang et al. (2011), further analysis was conducted that separates day–night overpasses and land–ocean cases. Four subgroups are shown in Fig. 8: daytime over land, daytime over ocean, nighttime over land, and nighttime over ocean. Qualitatively similar to the results in Wang et al. (2011), Fig. 8 shows that a larger diurnal cycle in convective buoyancy occurs over land than over ocean. The fraction of positive-buoyancy cases over land is larger at 1330 than that at 0130 LT. This is consistent with our understanding of the diurnal cycle of tropical convection. The buoyancy achieves its maximum at ~10 km. The change of the ratio of positive buoyancy over ocean from 6 to 10 km is smaller than that over land, possibly implying that melting-level distributions over land and ocean and thus the distributions of the latent heat release are different. Yuan et al. (2010) indicate that the levels where deep convective clouds are all in ice phase can be 2 km lower in altitude over ocean than over land, suggesting that convective cloud could gain more latent heat in lower levels, shedding light on the smaller changes of the ratio from 6 to 10 km over ocean in Fig. 8, especially the one at 1330 LT. For both the 0130 and 1330 LT curves in Fig. 8, the increase in the fraction of plumes with positive buoyancy from 6 to 8 km CTH is much larger over ocean than over land. This is consistent with the previous findings by Yuan et al. (2010) that land convection seldom glaciates at −15°C while ocean convection might do so.

6. Conclusions

A new method is presented to estimate the cloud-top temperature of convective clouds by correcting for the non-blackbody effect based on a relationship between cloud-top fuzziness (defined as the vertical distance between CTH and $\mathrm{ETH}_{10\mathrm{dB}Z}$) and the distance from cloud top to the cloud IR effective emission level. Figures 3 and 4 show the dependences of cloud-top radiative features on the CTF derived from both observations and radiative transfer model simulations. Using CTF measured by *CloudSat* cloud-profiling radar together with the IR brightness temperature (BT_{11}) from MODIS, the algorithm provides an estimate of the temperature of cloud top. Comparisons are made

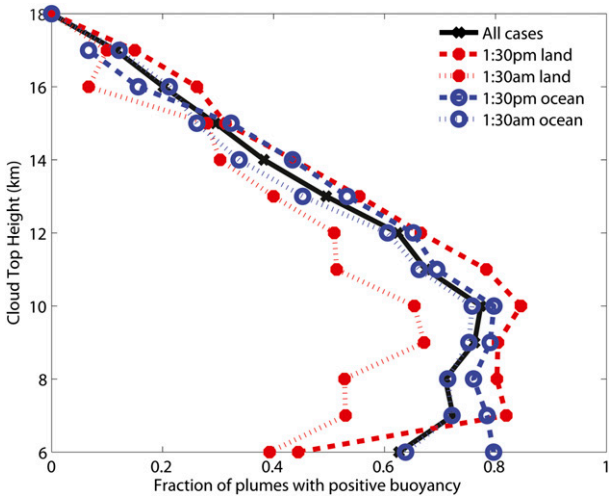

FIG. 8. Similar to Fig. 7. The black line is for all cases, and four subgroups are superimposed: daytime and nighttime over land (red lines) and daytime and nighttime over the oceans (blue lines). Dark dashed lines are for 0130 LT observations, and light-colored dashed lines are for 1330 LT observations.

with previous studies using the same datasets but a simple and less physically based method to correct for the non-blackbody effect. The new method is shown to outperform the old one. The major findings are summarized as follow:

1) Based on explicit radiative transfer model calculations, the mean effective emission level is at an IR optical depth (τ_{11}) of 0.72, lower than the value that is often assumed in atmospheric radiation lectures, which is 1. Among 16 837 cases examined, 99.4% of the effective emission level is in the range of τ_{11} at 0–2.
2) A regression relationship is developed that can parameterize the non-blackbody correction as a function of cloud-top fuzziness measured by *CloudSat* radar reflectivity profiles.
3) Using PCRTM, IWC, and LWC retrievals from *CloudSat* and *CALIPSO*, as well as ECMWF reanalysis datasets, we can largely reproduce the observed BT_{11} by MODIS, lending support to the validity of our method.

This new non-blackbody correction was applied to reevaluate the convective cloud-top buoyancy, as has previously been studied by Luo et al. (2010) and Wang et al. (2011). Results show that ~70% of the convective clouds observed by *CloudSat* as a snapshot in the height range of 6–10 km (i.e., apparent cumulus congestus) have positive buoyancy near cloud top, implying that they will continue to grow. This result underscores the importance of interpreting satellite snapshot observations as derived from polar-orbiting satellites with caution and within the proper dynamic context. Since the apparent cumulus congestus has a lot of vertical space to grow, previous statistics on this cloud type using snapshot observations should be reassessed. It should be noted that the information on cloud development is inferred from thermodynamic analysis (buoyancy analysis). To rigorously validate such inferences, an independent observation with high temporal resolution would be needed. Possible candidates for such observations include, but are not limited to, continuous Atmospheric Radiation Measurement Program ground radar observations, geostationary imagery in the window channels, and Multiangle Imaging Spectroradiometer (MISR) measurements, which observe the same cloud from different angles within a short time period. This investigation is a proof-of-concept study and such thorough and rigorous validations are beyond the scope of it. However, the validation is a focus of our follow-up studies.

It is worth mentioning the uncertainties associated with our analysis. This new non-blackbody correction is based on the fusion of multiple datasets, including satellite observations and retrievals as well as cloud-resolving model simulations. Thus, it is inevitably affected by the uncertainties and errors associated with these inputs. We described the uncertainties in the *CloudSat* retrievals and explained the choices we made in the face of them. We estimated some aspects of the uncertainties using Monte Carlo methods. However, to thoroughly and quantitatively pinpoint all uncertainties and to assess their impacts are beyond the scope of this study. This is especially true for the uncertainties of the parameters used in the cloud microphysics scheme of the GCE model. It would take tremendous computational effort to assess the full impact of the perturbations in these parameters. We acknowledge these limitations but at the same time stress the improvement of the new non-blackbody correction method in helping to estimate the cloud-top temperatures. The merit of data fusion in cloud remote sensing and analysis is also noted.

Acknowledgments. The *CloudSat* data were obtained from the *CloudSat* Data Processing Center. The MODIS data were obtained from NASA Goddard DISC. The ECMWF interim data used in this study were obtained online (http://data.ecmwf.int/data/). We thank all three reviewers for their insightful and thorough comments, which greatly improved the clarity of the article. This research is supported by the NASA MAP project under Grant NNX09AJ46G awarded to the University of Michigan, the NASA *CloudSat*/*CALIPSO* Science

Team under Grant NNX10AM31G, and the SEAC4RS Science Team under Grant NNX12AC13G, awarded to the City University of New York (CUNY).

REFERENCES

Casey, S. P. F., E. J. Fetzer, and B. H. Kahn, 2012: Revised identification of tropical oceanic cumulus congestus as viewed by CloudSat. *Atmos. Chem. Phys.,* **12,** 1587–1595, doi:10.5194/acp-12-1587-2012.

Deng, M., G. G. Mace, Z. Wang, and H. Okamoto, 2010: Tropical Composition, Cloud and Climate Coupling Experiment validation for cirrus cloud profiling retrieval using *CloudSat* radar and *CALIPSO* lidar. *J. Geophys. Res.,* **115,** D00J15, doi:10.1029/2009JD013104.

——, ——, ——, and R. P. Lawson, 2013: Evaluation of several A-Train ice cloud retrieval products with in situ measurements collected during the SPARTICUS campaign. *J. Appl. Meteor. Climatol.,* **52,** 1014–1030, doi:10.1175/JAMC-D-12-054.1.

Goody, R. M., and Y. L. Yung, 1995: *Atmospheric Radiation: Theoretical Basis.* 2nd ed. Oxford University Press, 519 pp.

Haynes, J. M., R. T. Marchand, Z. Luo, A. Bodas-Salcedo, and G. L. Stephens, 2007: A multi- purpose radar simulation package: QuickBeam. *Bull. Amer. Meteor. Soc.,* **88,** 1723–1727, doi:10.1175/BAMS-88-11-1723.

Johnson, R. H., T. M. Rickenbach, S. A. Rutledge, P. E. Ciesielski, and W. H. Schubert, 1999: Trimodal characteristics of tropical convection. *J. Climate,* **12,** 2397–2418, doi:10.1175/1520-0442(1999)012<2397:TCOTC>2.0.CO;2.

King, M. D., Y. Kaufman, W. P. Menzel, and D. Tanré, 1992: Remote sensing of cloud, aerosol, and water vapor properties from the Moderate Resolution Imaging Spectroradiometer (MODIS). *IEEE Trans. Geosci. Remote Sens.,* **30,** 2–27, doi:10.1109/36.124212.

Klemp, J. B., and R. B. Wilhelmson, 1978: The simulation of three-dimensional convective storm dynamics. *J. Atmos. Sci.,* **35,** 1070–1096, doi:10.1175/1520-0469(1978)035<1070:TSOTDC>2.0.CO;2.

Lang, S., W.-K. Tao, J. Simpson, and B. Ferrier, 2003: Modeling of convective–stratiform precipitation processes: Sensitivity to partitioning methods. *J. Appl. Meteor.,* **42,** 505–527, doi:10.1175/1520-0450(2003)042<0505:MOCSPP>2.0.CO;2.

Liu, X., W. L. Smith, D. K. Zhou, and A. Larar, 2006: Principal component-based radiative transfer model for hyperspectral sensors: Theoretical concept. *Appl. Opt.,* **45,** 201–209, doi:10.1364/AO.45.000201.

——, D. K. Zhou, A. M. Larar, W. L. Smith, P. Schluessel, S. M. Newman, J. P. Taylor, and W. Wu, 2009: Retrieval of atmospheric profiles and cloud properties from IASI spectra using super-channels. *Atmos. Chem. Phys.,* **9,** 9121–9142, doi:10.5194/acp-9-9121-2009.

Luo, Y., R. Zhang, W. Qian, Z. Luo, and X. Hu, 2011: Intercomparison of deep convection over the Tibetan Plateau–Asian monsoon region and subtropical North America in boreal summer using *CloudSat/CALIPSO* data. *J. Climate,* **24,** 2164–2177, doi:10.1175/2010JCLI4032.1.

Luo, Z., G. Y. Liu, and G. L. Stephens, 2008: *CloudSat* adding new insight into tropical penetrating convection. *Geophys. Res. Lett.,* **35,** L19819, doi:10.1029/2008GL035330.

——, ——, and ——, 2010: Use of A-Train data to estimate convective buoyancy and entrainment rate. *Geophys. Res. Lett.,* **37,** L09804, doi:10.1029/2010GL042904.

May, P. T., J. H. Mather, G. Vaughan, K. N. Bower, C. Jakob, G. M. McFarquhar, and G. G. Mace, 2008: The Tropical Warm Pool International Cloud Experiment. *Bull. Amer. Meteor. Soc.,* **89,** 629–645, doi:10.1175/BAMS-89-5-629.

McGill, M. J., L. Li, W. D. Hart, G. M. Heymsfield, D. L. Hlavka, P. E. Racette, L. Tian, M. A. Vaughan, and D. M. Winker, 2004: Combined lidar-radar remote sensing: Initial results from CRYSTAL-FACE. *J. Geophys. Res.,* **109,** D07203, doi:10.1029/2003JD004030.

Menzel, W. P., and Coauthors, 2008: MODIS global cloud-top pressure and amount estimation: Algorithm description and results. *J. Appl. Meteor. Climatol.,* **47,** 1175–1198, doi:10.1175/2007JAMC1705.1.

Minnis, P., P. W. Heck, and E. F. Harrison, 1990: The 27–28 October 1986 FIRE IFO cirrus case study: Cloud parameter fields derived from satellite data. *Mon. Wea. Rev.,* **118,** 2426–2447, doi:10.1175/1520-0493(1990)118<2426:TOFICC>2.0.CO;2.

——, C. R. Yost, S. Sun-Mack, and Y. Chen, 2008: Estimating the top altitude of optically thick ice clouds from thermal infrared satellite observations using *CALIPSO* data. *Geophys. Res. Lett.,* **35,** L12801, doi:10.1029/2008GL033947.

——, and Coauthors, 2012: Simulations of infrared radiances over a deep convective cloud system observed during TC4: Potential for enhancing nocturnal ice cloud retrievals. *Remote Sens.,* **4,** 3022–3054, doi:10.3390/rs4103022.

Niu, J. G., Y. Ping, H. L. Huang, J. E. Davies, J. Li, B. A. Baumc, and Y. X. Hu, 2007: A fast infrared radiative transfer model for overlapping clouds. *J. Quant. Spectrosc. Radiat. Transf.,* **103,** 447–459, doi:10.1016/j.jqsrt.2006.05.009.

Okamoto, H., S. Iwasaki, M. Yasui, H. Horie, H. Kuroiwa, and H. Kumagai, 2003: An algorithm for retrieval of cloud microphysics using 95-GHz cloud radar and lidar. *J. Geophys. Res.,* **108,** 4226, doi:10.1029/2001JD001225.

Platnick, S., M. D. King, S. A. Ackerman, W. P. Menzel, B. A. Baum, J. C. Riedi, and R. A. Frey, 2003: The MODIS cloud products: Algorithms and examples from *Terra*. *IEEE Trans. Geosci. Remote Sens.,* **41,** 459–473, doi:10.1109/TGRS.2002.808301.

Rossow, W. B., A. W. Walker, D. E. Beuschel, and M. D. Roiter, 1996: *International Satellite Cloud Climatology Project (ISCCP) Documentation of New Cloud Datasets.* WMO/TD-737, World Climate Research Programme, Geneva, Switzerland, 115 pp. [Available online at http://isccp.giss.nasa.gov/docs/documents.html.]

Sassen, K., Z. Wang, and D. Liu, 2009: Cirrus clouds and deep convection in the tropics: Insights from *CALIPSO* and *CloudSat*. *J. Geophys. Res.,* **114,** D00H06, doi:10.1029/2009JD011916.

Segelstein, D. J., 1981: The complex refractive index of water. M.S. thesis, Dept. of Physics, University of Missouri—Kansas City, 167 pp.

Sherwood, S. C., J.-H. Chae, P. Minnis, and M. McGill, 2004: Underestimation of deep convective cloud tops by thermal imagery. *Geophys. Res. Lett.,* **31,** L11102, doi:10.1029/2004GL019699.

Soong, S.-T., and Y. Ogura, 1980: Response of trade wind cumuli to large-scale processes. *J. Atmos. Sci.,* **37,** 2035–2050, doi:10.1175/1520-0469(1980)037<2035:ROTCTL>2.0.CO;2.

Stamnes, K., S. C. Tsay, W. Wiscombe, and K. Jayaweera, 1988: A numerically stable algorithm for discrete-ordinate-method radiative transfer in multiple scattering and emitting layered media. *Appl. Opt.,* **27,** 2502–2509, doi:10.1364/AO.27.002502.

Stephens, G. L., 1994: *Remote Sensing of the Lower Atmosphere: An Introduction.* Oxford University Press, 544 pp.

——, and Coauthors, 2002: The *CloudSat* mission and the A-Train: A new dimension of space-based observations of clouds and precipitation. *Bull. Amer. Meteor. Soc.,* **83,** 1771–1790, doi:10.1175/BAMS-83-12-1771.

——, and Coauthors, 2008: *CloudSat* mission: Performance and early science after the first year of operation. *J. Geophys. Res.,* **113,** D00A18, doi:10.1029/2008JD009982.

Takayabu, Y. N., S. Shige, W.-K. Tao, and N. Hirota, 2010: Shallow and deep latent heating modes over tropical oceans observed with TRMM PR spectral latent heating data. *J. Climate,* **23,** 2030–2046, doi:10.1175/2009JCLI3110.1.

Tao, W.-K., and J. Simpson, 1993: Goddard Cumulus Ensemble model: Part I. Model description. *Terr. Atmos. Ocean. Sci.,* **4,** 35–72.

——, and Coauthors, 2003: Microphysics, radiation and surface processes in the Goddard Cumulus Ensemble (GCE) model. *Meteor. Atmos. Phys.,* **82,** 97–137. [Available online at http://grims-model.org/front/bbs/paper/mps-4/MPS_2002-1_Tao_et_al.pdf.]

Wang, C., Z. J. Luo, and X. Huang, 2011: Parallax correction in collocating *CloudSat* and Moderate Resolution Imaging Spectroradiometer (MODIS) observations: Method and application to convection study. *J. Geophys. Res.,* **116,** D17201, doi:10.1029/2011JD016097.

Warren, S. G., 1984: Optical constants of ice from the ultraviolet to the microwave. *Appl. Opt.,* **23,** 1206–1225, doi:10.1364/AO.23.001206.

Wei, H., P. Yang, J. Li, B. A. Baum, H.-L. Huang, S. Platnick, Y. Hu, and L. Strow, 2004: Retrieval of semitransparent ice cloud optical thickness from Atmospheric Infrared Sounder (AIRS) measurements. *IEEE Trans. Geosci. Remote Sens.,* **42,** 2254–2267, doi:10.1109/TGRS.2004.833780.

Winker, D. M., M. A. Vaughan, A. H. Omar, Y. Hu, K. A. Powell, Z. Liu, W. H. Hunt, and S. A. Young, 2009: Overview of the *CALIPSO* mission and CALIOP data processing algorithms. *J. Atmos. Oceanic Technol.,* **26,** 2310–2323, doi:10.1175/2009JTECHA1281.1.

Wood, N., 2008: Level 2B Radar-Visible Optical Depth Cloud Water Content (2B-CWC-RVOD) process description document: Version 5.1. CloudSat Project Algorithm Theoretical Basis Doc., 26 pp. [Available online at http://www.cloudsat.cira.colostate.edu/ICD/2B-CWC-RVOD/2B-CWC-RVOD_PDD_V5p1.pdf.]

Xiong, X., B. N. Wenny, A. Wu, and W. L. Barnes, 2009: MODIS onboard blackbody function and performance. *IEEE Trans. Geosci. Remote Sens.,* **47,** 4210–4222, doi:10.1109/TGRS.2009.2023317.

Yang, P., B. Gao, B. A. Baum, Y. X. Hu, W. J. Wiscombe, S. Tsay, D. M. Winker, and S. L. Nasiri, 2001: Radiative properties of cirrus clouds in the infrared (8–13 μm) spectral region. *J. Quant. Spectrosc. Radiat. Transf.,* **70,** 473–504, doi:10.1016/S0022-4073(01)00024-3.

Young, A. H., J. J. Bates, and J. A. Curry, 2012: Complementary use of passive and active remote sensing for detection of penetrating convection from *CloudSat, CALIPSO,* and *Aqua* MODIS. *J. Geophys. Res.,* **117,** D13205, doi:10.1029/2011JD016749.

Yuan, T., J. V. Martins, Z. Li, and L. A. Remer, 2010: Estimating glaciation temperature of deep convective clouds with remote sensing data. *Geophys. Res. Lett.,* **37,** L08808, doi:10.1029/2010GL042753.

Zeng, X., W.-K. Tao, M. Zhang, A. Y. Hou, S. Xie, S. Lang, X. Li, D. Starr, X. Li, and J. Simpson, 2009: An indirect effect of ice nuclei on atmospheric radiation. *J. Atmos. Sci.,* **66,** 41–61, doi:10.1175/2008JAS2778.1.

——, ——, S. W. Powell, R. A. Houze Jr., P. Ciesielski, N. Guy, H. Pierce, and T. Matsui, 2013: A comparison of the water budgets between clouds from AMMA and TWP- ICE. *J. Atmos. Sci.,* **70,** 487–503, doi:10.1175/JAS-D-12-050.1.

Zuidema, P., 1998: The 600–800-mb minimum in tropical cloudiness observed during TOGA COARE. *J. Atmos. Sci.,* **55,** 2220–2228, doi:10.1175/1520-0469(1998)055<2220:TMMITC>2.0.CO;2.